ARTICLES

Treatment during a vulnerable developmental period rescues a genetic epilepsy

Stephan Lawrence Marguet[1–3,7], Vu Thao Quyen Le-Schulte[3,7], Andrea Merseburg[1–3], Axel Neu[3], Ronny Eichler[3], Igor Jakovcevski[1,2], Anton Ivanov[4], Ileana Livia Hanganu-Opatz[5], Christophe Bernard[4], Fabio Morellini[3,6] & Dirk Isbrandt[1–3]

The nervous system is vulnerable to perturbations during specific developmental periods. Insults during such susceptible time windows can have long-term consequences, including the development of neurological diseases such as epilepsy. Here we report that a pharmacological intervention timed during a vulnerable neonatal period of cortical development prevents pathology in a genetic epilepsy model. By using mice with dysfunctional Kv7 voltage-gated K+ channels, which are mutated in human neonatal epilepsy syndromes, we demonstrate the safety and efficacy of the sodium-potassium-chloride cotransporter NKCC1 antagonist bumetanide, which was administered during the first two postnatal weeks. In Kv7 current–deficient mice, which normally display epilepsy, hyperactivity and stereotypies as adults, transient bumetanide treatment normalized neonatal *in vivo* cortical network and hippocampal neuronal activity, prevented structural damage in the hippocampus and restored wild-type adult behavioral phenotypes. Furthermore, bumetanide treatment did not adversely affect control mice. These results suggest that in individuals with disease susceptibility, timing prophylactically safe interventions to specific windows during development may prevent or arrest disease progression.

Epilepsy is the most common neurological disorder after migraine, and in a quarter of cases it remains drug resistant[1], making the prevention of epileptogenesis a key clinical goal. The incidence of epilepsy is especially high in newborns and during the first years of life. Developing brains are vulnerable to insults and prone to seizures[2], but they may also be particularly amenable to prophylactic interventions that could protect at-risk individuals. Early brain development is tightly regulated by internal and external factors, such as transcription factors and sensory input. Internal perturbations (such as gene mutations) or external insults (such as hypoxia) that are not compensated for by homeostatic mechanisms[3] can lead to epilepsy, cognitive deficits or psychiatric disorders[4,5]. Critical periods are well established in sensory development and best characterized in the visual system, in which visual deprivation at specific times induces altered visual processing—a phenomenon that depends on the maturation of GABAergic signaling and a proper balance of excitation and inhibition[6–8]. We extend this notion to disease etiology and propose that some common neuropathologies, such as epilepsy, may be prevented by therapeutic interventions that are targeted to vulnerable periods during brain development.

We previously found a vulnerable early postnatal period for the pathogenic effects of a genetic neuronal channelopathy in mice. Animals deficient in functional Kv7 currents during the first two postnatal weeks later develop an epilepsy phenotype and pathological changes in brain structure and behavior[9]. Suppressing Kv7 currents before and after the first two postnatal weeks did not result in these pathological alterations. Neuronal Kv7 channels, which are voltage-gated potassium channels also known as M channels[10,11], are widely expressed in the brain[12] and are mainly localized to presynaptic compartments such as axon initial segments and axons[13]. They are of pathophysiological significance in humans, as mutations in *KCNQ2* and *KCNQ3*, which encode the Kv7.2 and Kv7.3 α-subunits of M channels, respectively, are associated with benign idiopathic epilepsy syndromes[14–17] and severe neonatal epileptic encephalopathy[18]. As in our animal model, and in contrast to benign syndromes such as benign familial neonatal convulsions (BFNC), encephalitic patients with Kv7 mutations tend to carry a dominant-negative mutation that probably leads to a more complete loss of M current and hence a stronger phenotype[19].

Using Kv7 current–deficient mice, we tested whether a prophylactic intervention restricted to a 2-week period of postnatal development could prevent the expression of an epilepsy phenotype. Barbiturates and other GABA mimetics are commonly administered to treat seizures after neonatal insults such as asphyxia, but these drugs control seizures in <50% of infants[20]. In addition, the prophylactic safety of these anticonvulsants is questionable[21]. Instead, we used

the loop diuretic and NKCC1 antagonist bumetanide as a model prophylactic[22] to arrest epileptogenesis, rather than treating already-manifest seizures[23,24].

Bumetanide treatment reduces the intracellular chloride concentration of immature cortical neurons *in vitro*, attenuating GABA-mediated depolarization[25]. In some models, bumetanide prevents hyperexcitability and suppresses seizure-like activity[23,24,26,27]. In a neonatal rat hypoxia-ischemia model, it augments the neuroprotective effects of combined hyperthermia and phenobarbital treatment[28]. In a critically ill human neonate with septic encephalitis and multifocal seizures, it also had anticonvulsive effects[29]. Instead of using bumetanide as an adjunct medication to improve the treatment of manifest epilepsy[30] (ClinicalTrials.gov identifier NCT00830531), we assessed whether bumetanide could normalize pathological activity and prevent epileptogenesis in our mouse model, before the manifestation of symptoms.

We hypothesized that Kv7 current dysfunction during the previously identified critical first two postnatal weeks[9] perturbs spontaneous electrical activity, which is thought to have an important role in brain maturation during this period[31–33]. Our present findings confirmed this hypothesis and revealed aberrant neuronal activity in 1-week-old neonates, without evidence for electrographic seizures. We thus tested whether normalizing network activity during this vulnerable period attenuates disease susceptibility, and used bumetanide not as an anticonvulsant but as a potential antiepileptogenic therapeutic. We furthermore assessed the safety of transient neonatal bumetanide therapy in control animals.

RESULTS

Kv7 channels control excitability in neonatal CA1 neurons

To model a neonatal epileptic encephalopathy that is linked to a genetic ion channelopathy, we generated mice that conditionally express a dominant-negative (nonconductive) Kv7.2 subunit transgene, whose product can co-assemble with endogenous Kv7 subunits to suppress neuronal Kv7-mediated M currents[9]. Mutations in the human *KCNQ2* gene that cause a similar loss of function of Kv7.2 subunits were associated with therapy-resistant epileptic encephalopathy in human neonates[19]. Because Kv7 subunits are already expressed in neonatal mouse brains[34,35], we first confirmed expression of the mRNA encoding the dominant-negative Kv7.2 subunit (Kv7DN) in the cerebral cortex and hippocampus of mutant (double-transgenic offspring of a mouse line that is transgenic for human *KCNQ2*[G279S] under the control of the tetracycline-response element, and another line that expresses the regulative tetracycline-responsive transcriptional activator (tTA) under the control of the prion protein promoter (Tg(*tetO-KCNQ2*[G279S]) × Tg(*Prnp-tTA*)F959Sbp/J))[9] embryos at day 17 of gestation (E17.5), shortly before birth. *KCNQ2*[G279S] mRNA levels were similar to those previously found in the adult mutant brain[9], indicating sufficient levels for effective suppression of endogenous Kv7 currents (**Fig. 1a**). Next we investigated whether electrophysiological properties of hippocampal neurons were altered in mutant neonates. At rest, control and mutant postnatal day 7 (P7) cornu ammonis 1 area (CA1) neurons did not differ in input resistance (controls: 580 ± 71 MΩ, $n = 17$ cells from five mice; mutants: 667 ± 55 MΩ, $n = 17$ cells from four mice; measured at -60 mV, $P = 0.34$) or resting membrane potentials (controls: -62.1 ± 0.7 mV, $n = 17$ cells from five mice; mutants: -60.6 ± 0.6 mV, $n = 17$ cells from four mice; $P = 0.13$). When injecting depolarizing current pulses into CA1 pyramidal cells from P6–P8 mice, we found that cells from mutant mice generated more action potentials per pulse and showed

weaker spike frequency adaptation than control neurons (**Fig. 1b**). In addition, the response to both the Kv7 channel activator retigabine and the Kv7 channel blocker XE991 was abolished in cells from mutant mice (**Fig. 1b**). Kv7 current amplitudes in CA1 pyramidal neurons from control hippocampal slices were comparable to those recorded from adult wild-type neurons[9]. In contrast, no significant Kv7 currents were detected in mutant neurons (**Fig. 1c** and **Supplementary Fig. 1**). These data establish that Kv7DN expression effectively abolishes endogenous Kv7 currents, resulting in hyperexcitability of CA1 pyramidal neurons during this vulnerable period of development.

Hippocampal inflammation in Kv7 mutants

We investigated whether the increased excitability of cells deficient in Kv7 currents led to network hyperactivity or its correlates, such as glial activation and inflammation. Immunohistochemical quantification of staining for the transcription factor c-Fos provides an indirect measure of recent neuronal activity[36]. At P14, the number of c-Fos–immunoreactive neurons was increased in the mutant CA1 pyramidal layer but not in the CA3 layer or the dentate gyrus (DG), as compared to littermate controls (**Fig. 1d**; $n = 3$ for both genotypes; 6 hippocampal sections per animal). By using the astrocyte marker glial fibrillary acidic protein (GFAP), we observed reactive astrogliosis in the hippocampi of mutant mice. Marked GFAP staining was present in the entire adult hippocampus, but especially in the CA1 and DG regions (**Fig. 1e**; $n = 5$ per genotype). In contrast to the large area of GFAP immunoreactivity, isolectin B4+ staining, indicative of activated microglia and neuroinflammation[37], was restricted to CA1 pyramidal and DG granule cell layers (**Fig. 1e**).

When analyzed as adults, mutants expressing Kv7DN throughout their lives had neuronal dispersion and cell loss in the hippocampal CA1 pyramidal layer[9] (**Fig. 1e**). In neonatal mutant mice, CA1 cell dispersion was detectable as early as the first week of life (P5–P7 mice; $n = 7$ for Nissl stains), whereas no microglial activation and only slight reactive astrogliosis were detectable at this age (**Fig. 1e**, $n = 3$ for GFAP and isolectin B4 stains). These findings link attenuated Kv7 current amplitudes to altered neuronal activity and to neuropathological changes localized to the CA1 pyramidal cell layer. They further confirm the first two postnatal weeks as the vulnerable window during which Kv7 dysfunction can lead to long-term neuropathological changes[9], because suppressing the expression of the transgene encoding Kv7DN with doxycycline (Dox) during the first one or two weeks of life was sufficient to prevent both neuronal dispersion[9] and inflammation in adult mutants (**Fig. 1e**), despite lifelong post-weaning Kv7 channelopathy.

In vitro hippocampal network activity is unchanged by Kv7 current deficiency

We next assessed whether neuronal hyperexcitability translated to aberrant network activity. Analysis of spontaneous 'giant depolarizing potentials' (GDPs) from CA3 neurons in acute brain slice preparations of P5–P7 mutant or control mice did not reveal any differences (**Supplementary Fig. 2**, $n = 7$ for both genotypes). We then performed *in vitro* recordings of spontaneous extracellular field potentials in the CA1 layer of isolated hippocampi from P13 mice[38]. Both control and mutant hippocampi showed delta-like local field potential (LFP) oscillations centered around 1.5 Hz with no differences in oscillation frequency (**Supplementary Fig. 3**). These results show that spontaneous autonomous network activity in hippocampal neonatal *in vitro* preparations, which is predominantly generated in the CA3 region[38,39], was unaltered in mutant mice.

In vivo network activity is altered in Kv7-deficient neonates

Next we investigated the effect of attenuated Kv7 currents on *in vivo* hippocampal and cortical network activity at P5–P7, and on CA1 neuronal spiking at P10–P11 in awake, head-fixed mice. We recorded LFPs at P5–P7, the first time points of observable CA1 cell dispersion, along the CA1–dentate gyrus axis using linear 16-site silicon probes (**Supplementary Fig. 4**). We observed two prominent activity patterns in the neonatal hippocampus of both controls and mutants: sharp waves with a phase reversal in the CA1 pyramidal layer and short-lasting oscillations in the 10–30 Hz (beta) frequency (hippocampal beta oscillations (HBOs); **Supplementary Fig. 5a–f**). Depth profiles of sharp waves were comparable to those described in rat pups[40], and both events could co-occur with spontaneous limb twitches (**Supplementary Fig. 5g**). Current-source-density (CSD) analysis

revealed similar current sinks for both sharp waves and HBOs, indicating either CA3 pyramidal cell activity via Schaffer collateral projections to CA1 (ref. 40) or excitation via the perforant pathway from the entorhinal cortex (**Supplementary Fig. 5a,b,d,e**). Quantitative analysis of *in vivo* hippocampal network recordings in control and mutant mice revealed similar sharp wave rates and amplitudes, and similar HBO occurrence rates, mean lengths and peak frequencies (**Supplementary Fig. 5h**). These findings suggest that spontaneous afferent input onto CA1 apical dendrites in the mutants was unaltered, consistent with the lack of changes in intrinsic CA3-dependent oscillations seen *in vitro* (**Supplementary Figs. 2** and **3**).

We next quantified the CA1 output (i.e., the spontaneous unit activity in the CA1 pyramidal layer) of slightly older (P10–P11) animals using electrodes optimized to isolate single units (see Online Methods).
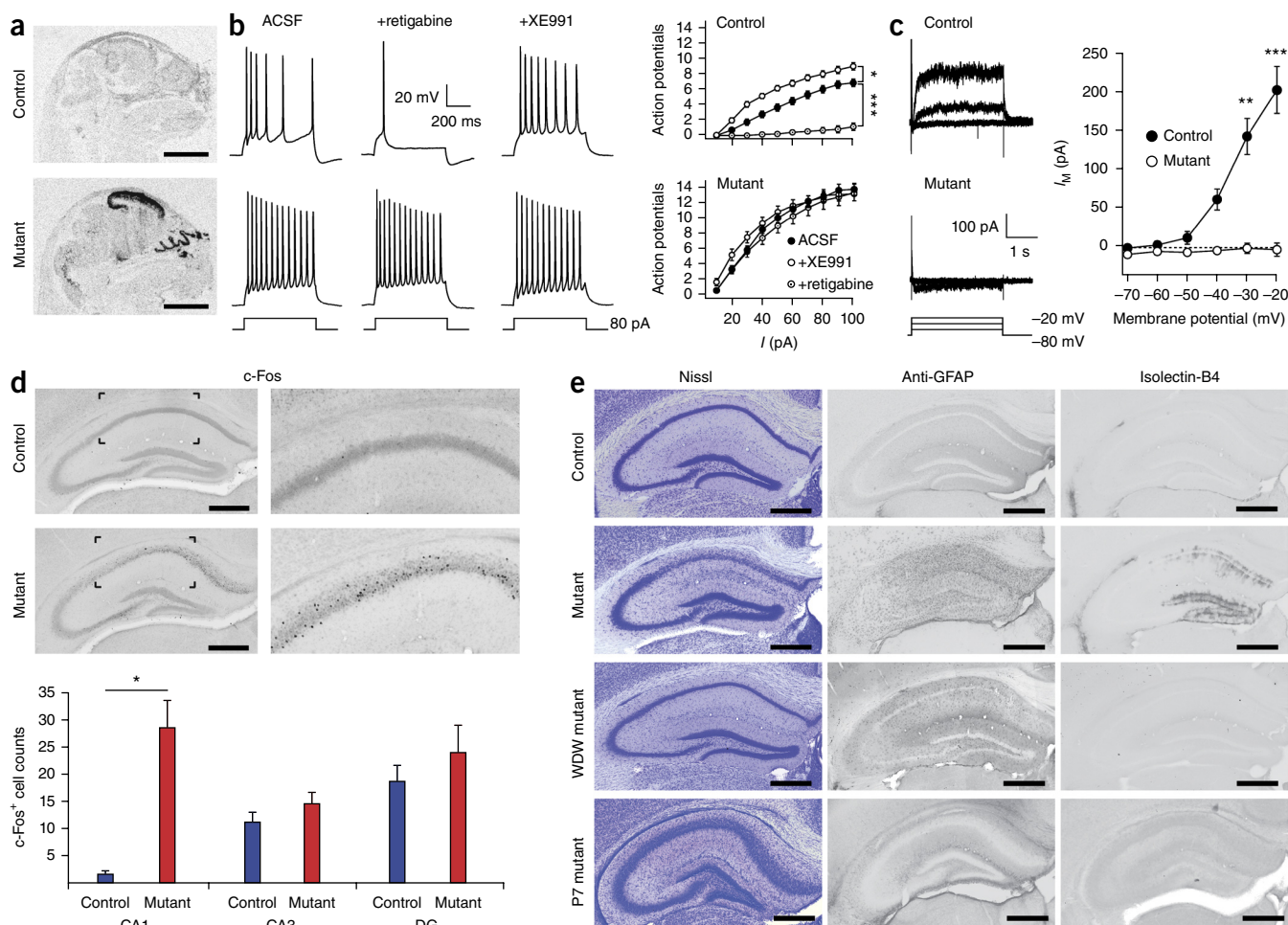

Figure 1 Altered hippocampal excitability and structure induced by Kv7 channelopathy. (**a**) *In situ* hybridization of Kv7DN-encoding mRNA in E17.5 control (top) and mutant (bottom) embryos. Scale bars, 200 μm. (**b**) Representative current-clamp recordings and quantification (graphs) from CA1 pyramidal neurons of P7 control ($n = 11$ cells from four mice, top) and mutant ($n = 19$ cells from four mice, bottom) mice showing depolarizations induced by 80-pA current injection at baseline (left traces) or in the presence of retigabine (middle traces) or XE991 (right traces). *$P < 0.05$, ***$P < 0.001$; Newman-Keuls post hoc test after three-way mixed ANOVA (genotype × treatment: $F_{2,651}$; $P < 0.01$). (**c**) Current-voltage (*I-V*) relationship of the XE991-sensitive current recorded (left) and quantified (right) from control (left, top) and mutant (left, bottom) cells showing M current amplitudes (controls and mutants $n = 10$ cells from three mice; **$P < 0.01$, ***$P < 0.001$, as compared to mutants at the same membrane potential by Newman-Keuls post hoc after two-way mixed ANOVA. (**d**) Top, representative images of c-Fos immunostaining of the hippocampal region from control (top, $n = 3$) and mutant (bottom, $n = 3$) P14 mice. CA1 areas (boxed regions, left) are magnified at right. Bottom graph, quantification of c-Fos+ cells in control and mutant P14 mice ($n = 3$ each) in the CA1, CA3 and dentate gyrus regions (bottom). Scale bars, 500 μm. *$P < 0.05$; Kruskal-Wallis one-way ANOVA. (**e**) Coronal Nissl- (left), GFAP- (middle) and isolectin B4–stained (right) sections through the dorsal hippocampus of adult control (top row), adult mutant (second row), adult water-dox-water (WDW; which corresponds to the suppression of transgene expression by doxycycline administration for just the first two postnatal weeks)[9] mutant (third row) and neonatal (P7; bottom row) mutant mice. Each row shows adjacent brain sections from the same animal. Scale bars, 500 μm. Throughout, error bars represent mean ± s.e.m.

Figure 2 Abnormal spontaneous *in vivo* network activity in neonatal mutants. (**a**) Representative traces of *in vivo* hippocampal extracellular unit recordings obtained from P11 control (top) and mutant (bottom) mice, highlighting particularly bursty hippocampal cells (different units indicated by colored tick marks). (**b**) Auto-correlograms (ACG; single-sided, log-scaled) for the identically colored neurons in **a**, illustrating prominent primary and secondary burst-related peaks for neurons from control (top) and mutant (bottom) mice. Insets show amplitude-normalized average unit waveforms for the corresponding bottom two channels of the traces from control and mutant mice in **a** (black, gray). (**c**) Summary histograms (top) and boxplots (bottom; black median surrounded by colored 25th–75th percentile box, whiskers indicate theoretical 99% confidence; '+' are outliers) of hippocampal unit activity. Left, distribution of first ACG peaks under 25 ms (identifiable in over half of all recorded units; $n = 87$ units from seven control mice; $n = 70$ units from five mutant mice). Middle and right, distribution of unit burst spiking defined as spikes occurring in triplets (middle) or quadruplets (right) with inter-spike intervals between 2 and 15 ms (triplets and quadruplets, $n = 151$ units from eight control mice; $n = 117$ units from five mutant mice). ***$P < 0.001$; Mann-Whitney U test. (**d**) Spectrogram of the CSD constructed from channels ~150 µm deep in an acute silicon probe depth-profile recording in the V1 cortex of a P7 control mouse. Activity corresponding to spontaneous bursts of spindle-like oscillations (spindle bursts, SBs) is indicated by the rectangular ticks. (**e**) Left, 10- to 30-Hz LFP spectrogram (from channel

2) of a recording channel 100 µm deep during the event shown on the right. Right, LFP traces of the top four recording channels (50–200 µm deep) showing spontaneous SBs in the low beta-frequency range at 5 min in **d** and highlighted in the spectrogram on the left. (**f**) SB rates in the V1 cortex of control and mutant genotypes ($n = 12$ controls and $n = 14$ mutants; *$P < 0.05$; unpaired *t*-test). Throughout, error bars represent mean ± s.e.m.
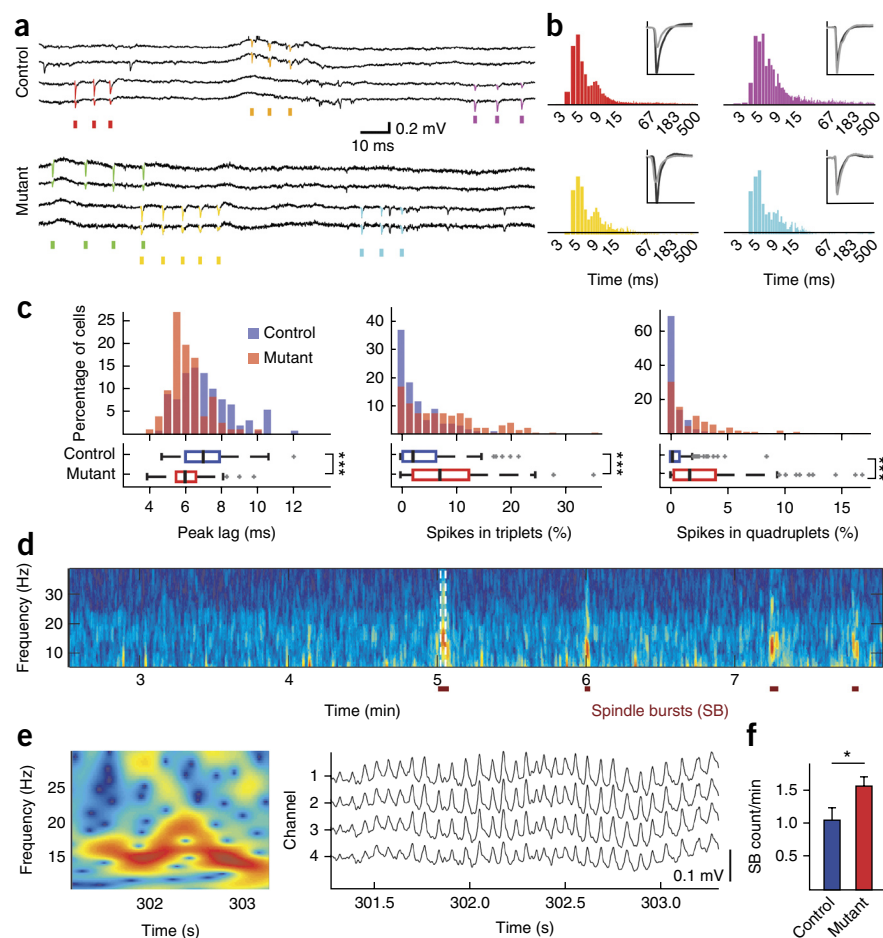
Offline processing of wide-band recordings from head-fixed neonates yielded 268 units from 13 animals. Although the average single-unit firing rates of control and mutant putative pyramidal neurons did not differ (**Supplementary Fig. 6a**), the distributions of firing patterns diverged. Neurons in Kv7-deficient mice were more likely to show increased burstiness (**Supplementary Fig. 6b**), firing more action potentials in bursts of two or more spikes with intervals of 2–15 ms (**Fig. 2a**–**c**). The burst interval, suggested by the first strong peak in the auto-correlogram (when present, as in over 50% of cells for both genotypes; **Fig. 2b**,**c**), was also significantly shorter in mutants. Differences between genotypes were also pronounced when assessing the fraction of cells with high amounts of triplet or quadruplet burst sequences (consecutive spikes with 2- to 15-ms intervals, **Fig. 2c**; or as quadruplets and quintuplets in short time windows, **Supplementary Fig. 6c**). Together with the increased c-Fos immunoreactivity that was detected in the CA1 pyramidal layer (**Fig. 1d**), these electrophysiological findings indicate altered spiking activity of mutant CA1 neurons.

Because Kv7 channel subunits are also expressed in the cortex[12,13], we investigated whether activity was modified in cortical networks. Prior to eye opening, the intrinsic spontaneous activity of rat primary visual (V1) cortex consists of 'spindle burst' oscillations in superficial cortical layers[33], reflecting intrinsic cortical excitability. In control P5–P7 mice, these oscillations had frequencies in the beta range

(10–30 Hz) (**Fig. 2d**,**e**) and were variable in duration, with most events lasting less than 5 s and only a few exceeding 20 s (**Supplementary Fig. 7d**). As previously described in infant rats and humans[41,42], the V1 cortex also displayed slow activity transients (**Supplementary Fig. 7e**). Similar LFP patterns and no seizure activity were observed in mutant mouse pups (**Supplementary Fig. 7**). Spindle bursts had comparable spectral peak frequencies and durations (**Supplementary Fig. 7d**); however, the rate of spindle bursts in the V1 cortex was increased in the mutants (**Fig. 2f**). Our neonatal *in vivo* recordings revealed network hyperactivity in the V1 cortex and altered unit firing in the hippocampus.

Postnatal NKCC1 blockade is therapeutically safe in mice

Because we observed altered network activity in the same postnatal period during which Kv7DN expression is necessary for the expression of the adult phenotype[9], we reasoned that normalizing early network activity—before the manifestation of seizures or gross morphological damage—could help arrest or mitigate the process of epileptogenesis. During this critical phase of development, GABA can facilitate excitation in cortical neurons that have high intracellular chloride[43]. We thus conjectured that attenuation of GABA-mediated depolarization and/or reinforcing its hyperpolarizing action through NKCC1 blockade with the loop diuretic bumetanide might normalize network activity. To test this hypothesis, we subcutaneously injected
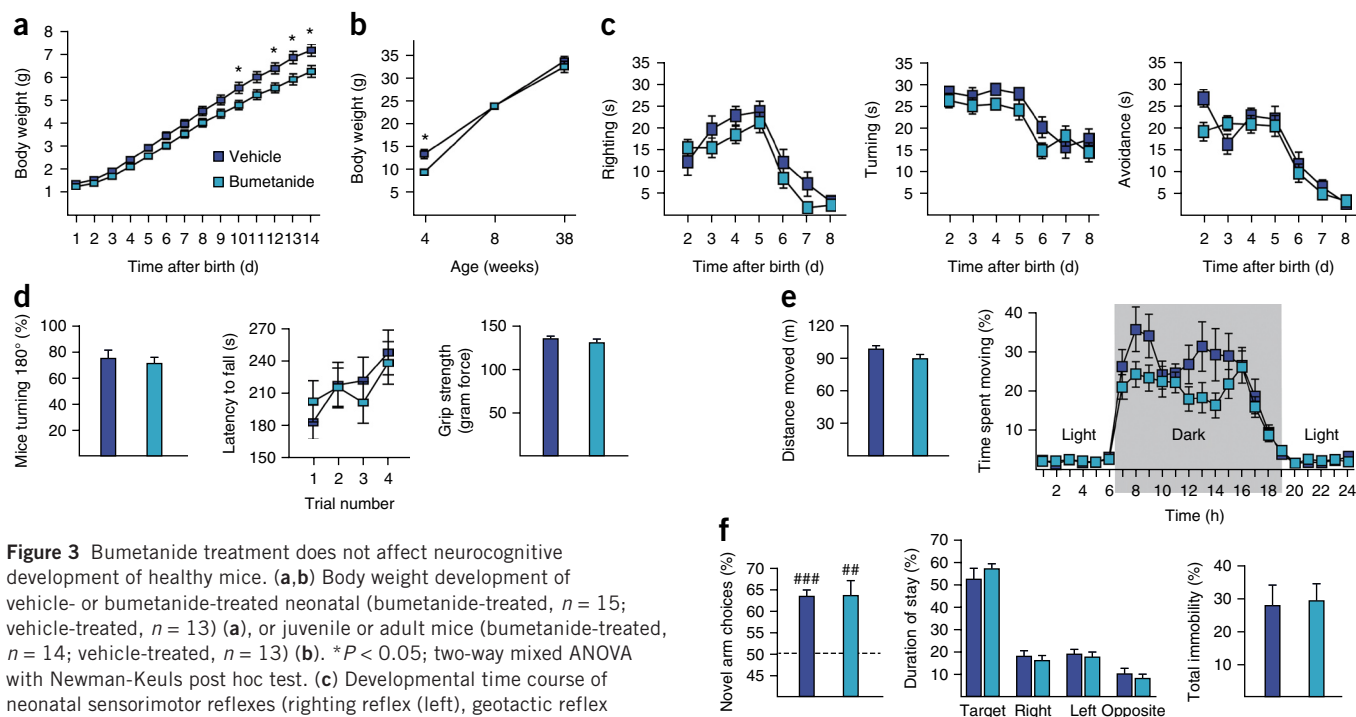
Figure 3 Bumetanide treatment does not affect neurocognitive development of healthy mice. (**a,b**) Body weight development of vehicle- or bumetanide-treated neonatal (bumetanide-treated, $n = 15$; vehicle-treated, $n = 13$) (**a**), or juvenile or adult mice (bumetanide-treated, $n = 14$; vehicle-treated, $n = 13$) (**b**). *$P < 0.05$; two-way mixed ANOVA with Newman-Keuls post hoc test. (**c**) Developmental time course of neonatal sensorimotor reflexes (righting reflex (left), geotactic reflex (middle) and cliff avoidance behavior (right)) in bumetanide- ($n = 19$) or vehicle-treated ($n = 13$) pups. (**d**) Motor coordination in adult mice tested with the pole (left), rotarod (middle) and grip strength (right) tests. (**e**) Locomotor activity measured in the open-field (left) and home cages (right; periods of light and dark are indicated). (**f**) Cognitive behavior in Y maze (left) and water maze (middle), and after contextual fear conditioning (right) (vehicle-treated, $n = 13$; bumetanide-treated, $n = 14$ for home cage activity and fear conditioning tests; $n = 15$ for pole, rotarod, grip strength, open-field cage, Y maze and water maze tests) ##$P < 0.01$, ###$P < 0.001$; in Y maze test, as compared to chance (50%, dashed line); Wilcoxon signed-rank test. Colored boxes are as in **a**. Throughout, error bars represent mean ± s.e.m.

mice with bumetanide from P0 to P14, twice per day at a concentration of 0.2 mg per kg body weight (mg/kg). Because a recent study has suggested that chronic bumetanide treatment from E15 until P14 has adverse effects[44], we investigated the potential side effects of bumetanide treatment from P0–P14 in controls to test its prophylactic safety. Neonates and juvenile mice were assessed for body weight (**Fig. 3a,b**) and reflex development (**Fig. 3c**). Adult behavior was characterized by quantifying motor coordination (**Fig. 3d**), spontaneous locomotor activity (**Fig. 3e**) and cognitive performance (**Fig. 3f**). From P10 until 4 weeks of age, bumetanide-treated mice showed a reduction in body weight, as compared to vehicle-treated mice; however, by 8 weeks of age the weight differences were undetectable (**Fig. 3a,b**). Because vehicle- and bumetanide-treated control mice showed indistinguishable behavior and performance in all of the tests (**Fig. 3c–f**), we conclude that neonatal P0–P14 bumetanide treatment of control mice did not impair neurocognitive development.

NKCC1 blockade normalizes mutant *in vivo* network activity

Next we investigated the effect of twice-daily bumetanide treatment on spontaneous *in vivo* cortical and hippocampal LFPs and on hippocampal unit activities in 1- to 2-week-old mice. Bumetanide treatment reduced c-Fos immunoreactivity in the CA1 pyramidal layer and normalized the firing pattern distributions of mutant hippocampal neurons, without altering the firing properties of control neurons (**Fig. 4a,b** and **Supplementary Fig. 8**). Two-way analysis of variance (ANOVA) (with genotype and treatment as 'between group' factors) revealed a significant effect of genotype on HBO rate ($F_{1,33} = 8.5$; $P < 0.01$) and length ($F_{1,33} = 5.3$; $P < 0.05$) in the treatment groups (**Supplementary Fig. 9**), which was not observed in unhandled pups (**Supplementary Fig. 5**). Bumetanide effects on LFP activity in the

hippocampus of twice-daily-treated animals approached, but did not reach, significance (effect on HBO rate: $F_{1,33} = 3.3$, $P = 0.08$; effect on HBO length: $F_{1,33} = 3.5$, $P = 0.07$; **Supplementary Fig. 9**).

We then investigated the effect of bumetanide treatment on cortical network activity. There was a significant effect of the interaction between genotype and treatment on the rate of V1 spindle bursts ($F_{1,33} = 7.3$; $P < 0.05$); Newman-Keuls post hoc analyses indicated that the rate was elevated in vehicle-treated mutants as compared to controls or bumetanide-treated mutants (**Fig. 4c**). Thus, as previously seen in untreated mice (**Fig. 2f**), the rate of V1 spindle bursts was elevated in mutants, but twice-daily bumetanide application normalized mutant V1 cortical hyperactivity without significantly changing activity levels in controls. Together, our data show a significant and selective normalizing effect of bumetanide on cortical network hyperactivity and on altered hippocampal firing patterns in mutants.

Neonatal NKCC1 blockade prevents structural and behavioral pathology

Because twice-daily bumetanide treatment effectively normalized cortical network activity and hippocampal firing patterns in 1- to 2-week-old mutant mice, we subsequently assessed the long-term effects of treating the mice just during the first two neonatal weeks. At 6–8 weeks of age, certain mutant behavioral abnormalities (such as stereotypic and tail-catching behavior, as well as stargazing[9]) were qualitatively absent in bumetanide-treated mutants. Hyperactivity in the home cage and novelty-induced open-field hyperactivity were significantly reduced (**Fig. 5**). The efficacy of bumetanide treatment suggested hyperactivity of GABA signaling during mutant brain development. We thus tested the efficacy of treating with a non-epileptic dosage (0.1 mg/kg) of the GABA type A (GABA$_A$) receptor

Figure 4 Timed bumetanide treatment normalizes *in vivo* unit and network activity. (**a**) Left, representative images of c-Fos expression in the CA1 layer in vehicle (Veh)- (left) or bumetanide (Bum)-treated (right) mutants. Right, quantification of vehicle- or bumetanide- treated mutants and controls (averaged over four slices per animal, left and right hemispheres; *n* = 4 for each mutant group; *n* = 2 for each control group). Scale bars, 100 μm. (**b**) Top, summary histograms and box plots (bottom of each set of graphs; black median surrounded by colored 25th–75th percentile box, whiskers indicate theoretical 99% confidence; '+' are outliers) for the effect of bumetanide treatment on the distribution of mutant hippocampal spiking patterns. Columns show ACG peak latencies (*n* = 70 units from five vehicle-treated mutant mice; *n* = 79 units from seven bumetanide-treated mutant mice) (left), and the distribution of cells' triplet (middle; two short inter-spike intervals) and quadruplet (right; three short inter-spike intervals) spikes (*n* = 117 units from five vehicle-treated mutant mice; *n* = 145 units from eight bumetanide-treated mutant mice). Bottom, P11 hippocampal bursting in control animals (ACG analysis: *n* = 87 units from seven vehicle-treated control

mice; *n* = 101 units from six bumetanide-treated control mice; triplets and quadruplets: *n* = 151 units from seven vehicle-treated control mice; *n* = 186 units from seven bumetanide-treated control mice). (**c**) Quantification of cortical spindle burst (SB) occurrence rate in *in vivo* recordings from vehicle- or bumetanide-treated controls or mutants (vehicle-treated controls, *n* = 8; bumetanide-treated controls, *n* = 11; *n* = 9 each for vehicle- or bumetanide-treated mutants). There was a significant effect of the interaction between genotype and treatment on the rate of V1 spindle bursts; the rate was elevated in vehicle-treated mutants compared to vehicle- or bumetanide-treated controls and bumetanide-treated mutants. Throughout, error bars represent mean ± s.e.m.; **P < 0.01, ***P < 0.001; Kruskal-Wallis one-way ANOVA with post hoc Kruskal-Wallis multiple comparisons test.

antagonist picrotoxin (Ptx) administered during the same 2-week postnatal period. This treatment improved, but did not completely normalize, hippocampal structural changes and behavioral

hyperactivity (**Supplementary Fig. 10**). A third treatment aimed at reducing general neurotransmitter release using levetiracetam administration did not prevent behavioral abnormalities, although
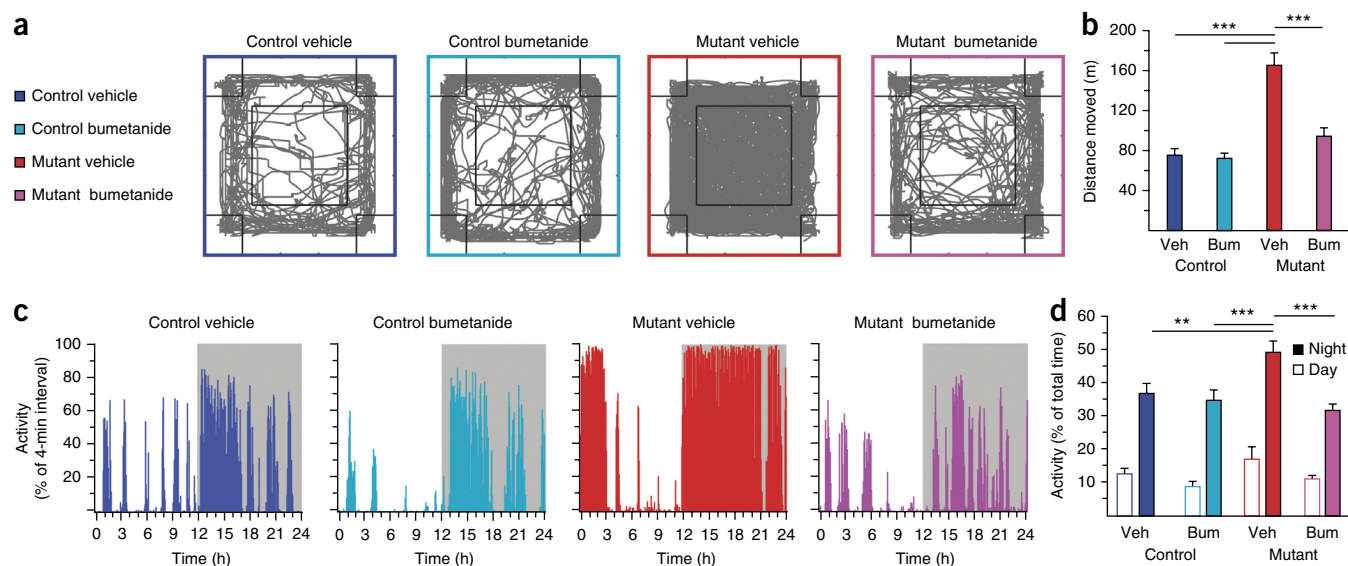

Figure 5 Prophylactic bumetanide treatment during a vulnerable window protects against behavioral hyperactivity. (**a**) Sample activity patterns of 15-min open-field experiments of vehicle- or bumetanide-treated control and mutant mice. (**b**) Quantification of open-field behavior during a 15-min test period with respect to overall distance moved (*n* = 10 for all groups). ***P < 0.001; two-way ANOVA with Newman-Keuls post hoc test. (**c**) Sample activity patterns during 24-h periods consisting of 12 h of daylight and 12 h of darkness (gray background) of vehicle- or bumetanide-treated control and mutant mice. Only vehicle-treated mutants showed increased home cage activity during the night and at the beginning of the day. (**d**) Quantification of mean home cage activity during 12-h intervals of day and night revealing a reduction in the increase in activity levels in bumetanide-treated, as compared to vehicle-treated, mutant mice (*n* = 10 for all groups). **P < 0.01, ***P < 0.001; three-way mixed ANOVA with Newman-Keuls post hoc test. Throughout, error bars represent mean ± s.e.m.

Figure 6 Bumetanide treatment restores hippocampal structure and reduces neuroinflammation and abnormal ECoG events. The hippocampal sections were stained as in **Figure 1e**; each row shows adjacent sections from the same animal. (**a**) Representative coronal Nissl- (top), GFAP- (middle) or isolectin B4–stained (bottom) sections through the hippocampal region of adult mutant (left, right) and control (middle) mice after neonatal (P0–P14) vehicle (left, middle) or bumetanide (bum; right) treatment showing absence of both CA1 pyramidal layer dispersion and inflammation in bumetanide-treated mutants (n = 5 for each group). Scale bars, 500 µm. (**b**,**c**) Representative immunoblotting (**b**) and corresponding quantification of the ratio (**c**) of GFAP and synaptophysin immunoreactivities in hippocampal brain lysates from vehicle- or bumetanide-treated control and mutant mice (n = 3 for each group). *$P < 0.05$; Kruskal-Wallis one-way ANOVA with Dunn's multiple comparisons test. (**d**) Representative spectrograms from two animals showing a high-amplitude event bordered by the dashed lines. Bottom spectrograms from each set show zoomed wavelet and overlaid telemetric traces (with time units as 'seconds past the hour'). Events exhibiting 5–10 Hz of spectral power were detected; they lasted 2–10 s long and were only present in mutants. (**e**) Quantification of high-amplitude events, which were found to be present in all vehicle-treated mutants (n = 6) but present in only 2 of 11 bumetanide-treated mutants. **$P < 0.01$, ***$P < 0.001$; Kruskal-Wallis one-way ANOVA with Kruskal-Wallis multiple comparisons test. Throughout, error bars represent mean ± s.e.m.
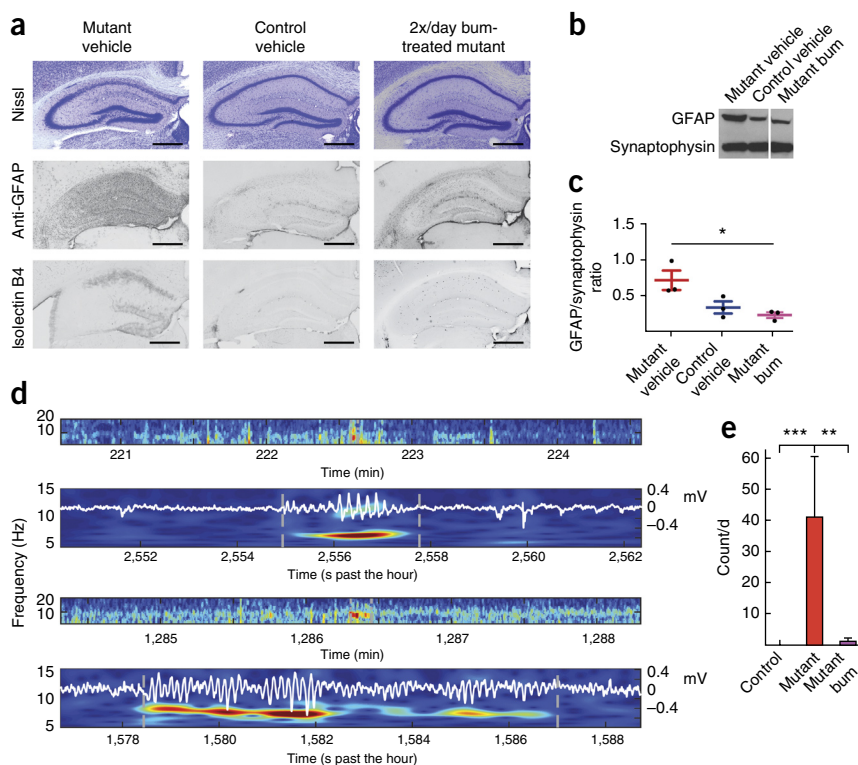
the target of levetiracetam, the synaptic vesicle glycoprotein 2A (SV2A), is already expressed at early stages of development[45] (**Supplementary Fig. 10**).

At 10–12 weeks of age, bumetanide-treated mutants were nearly indistinguishable from vehicle-treated controls with respect to hippocampal structure, GFAP and isolectin B4 immunoreactivity in fixed tissue sections (**Fig. 6a**), or GFAP expression in hippocampal tissue lysates (**Fig. 6b,c**). Notably, the bumetanide effect on microglial activation was dose dependent, because a single injection per day (0.2 mg/kg) resulted in a reduction, but not in complete prevention, of isolectin B4 immunoreactivity in the CA1 layer and DG of mutant mice (**Supplementary Fig. 11**). To investigate the long-term effects of postnatal bumetanide treatment of mice on cortical excitability, we performed telemetric electrocorticogram (ECoG) recordings from the sensorimotor cortical region of adult animals. Because we did not observe generalized seizures during the recording period of at least 72 h/mouse, we quantified the occurrence of spontaneous 5–10 Hz hypersynchronous episodes (**Fig. 6d**), which probably reflect increased thalamocortical excitability and focal motor seizures[46,47]. These episodes were detected in all vehicle-treated mutants but were absent in controls as well as 9 of 11 bumetanide-treated mutants (**Fig. 6e**).

Altogether, our data provide evidence that transient neonatal bumetanide treatment effectively prevents long-term Kv7 dysfunction-associated hippocampal structural changes, and behavioral and electrophysiological alterations.

DISCUSSION

In this study, we provide the first proof of concept that prophylactic pharmacological treatment during a vulnerable developmental period can prevent a channelopathy-induced encephalopathy, despite the continued presence of the underlying ion channel dysfunction. This highlights the importance of identifying possible windows of prophylactic efficacy for disease prevention. Our previous results implied that a potential treatment window might be very brief, as restoring Kv7 channel function after weaning did not prevent the appearance of the phenotype[9]. The results suggested that developing neural networks are vulnerable to specific perturbations during the first postnatal weeks, which can result in the emergence of severe adult phenotypes[9]. Here we show abnormal activity in hippocampus and cortex during the identified Kv7 vulnerable time window and demonstrate the long-term effectiveness of an activity-normalizing treatment that is restricted to the same period. Targeting GABA signaling by transient NKCC1 blockade with bumetanide prevented the development of chronic structural, physiological and behavioral changes. In control littermates, neonatal bumetanide application did not significantly alter the principle network activity or unit firing patterns, nor did it impair brain or cognitive development. The effect of bumetanide on physiological and pathological activity in developing networks, both *in vitro* and *in vivo*, is ambiguous. Differing results obtained from varied models and the scarcity of *in vivo* data have prompted questions regarding the applicability of bumetanide[48,49], and definitive *in vivo* proof of efficacy and safety has yet to be established[30]. In particular, concerns have been raised about its potential ototoxicity[30] and applicability in neonatal epilepsy[48,49], as only a few *in vivo* studies have been published so far, and the pharmacokinetic properties of bumetanide indicate limited penetration of the blood-brain barrier and fast metabolization[50–52]. Although bumetanide treatment did not alter cortical *in vivo* network activity in wild-type rat pups[53], it reduced hippocampal LFP power during kainate-induced seizures in neonatal

rats[23], prevented the induction of ectopic dentate granule cells in a rat neonatal febrile seizure model[22] and had anticonvulsive effects in a human neonate with septic encephalopathy[29]. In neonatal *in vitro* slice preparations, application of bumetanide attenuated GDP generation by CA3 neurons[35], but the effect of bumetanide in slice epilepsy models was dependent on the model chosen and was different for ictal-like versus interictal-like activity[23,24,26,27,54]. Although another recent study has suggested that bumetanide treatment for extended pre- and postnatal periods may impair brain development in mice[44], bumetanide treatment was beneficial for improving the balance between hippocampal excitation and inhibition in rodent models of autism[55] and Down syndrome[56].

In contrast to ongoing or completed clinical trials for neonatal seizures, our study was not aimed at investigating the acute anticonvulsive properties of bumetanide. We instead focused prophylactic treatment to a specific time window—the postnatal susceptibility period of our Kv7 channelopathy mouse model. Our data link altered cortical network and hippocampal unit activity in the neonatal mouse brain to structural and functional outcome in adulthood. The beneficial effects of targeting GABA signaling by NKCC1 or GABA$_A$ receptor blockade in a susceptible newborn period implicates early GABA$_A$ receptor-mediated activity in the pathophysiology of the Kv7 epileptic encephalopathy model. Our findings suggest that attenuating intracellular chloride accumulation via NKCC1 blockade, or potentially potassium-chloride transporter 2 (KCC2) activation[57], can be protective. Because both hypoxia and brain trauma can also raise intracellular chloride and shift the reversal potential for GABA$_A$ receptor–mediated responses[58,59], modifying chloride balance may prove to be a promising therapy that can be targeted to critical treatment windows in the genesis of other diseases.

METHODS

Methods and any associated references are available in the online version of the paper.

Note: Any Supplementary Information and Source Data files are available in the online version of the paper.

AUTHOR CONTRIBUTIONS

S.L.M. and V.T.Q.L.-S. contributed equally to the manuscript. D.I. conceived the study. D.I., S.L.M., C.B. and V.T.Q.L.-S. wrote the manuscript. V.T.Q.L.-S., I.L.H.-O. and D.I. established experimental conditions for *in vivo* electrophysiological experiments and performed the initial data analysis. S.L.M., V.T.Q.L.-S. and D.I. performed—and S.L.M., V.T.Q.L.-S., A.M. and D.I. analyzed—all *in vivo* electrophysiological experiments. S.L.M. wrote Matlab routines for data analysis and graphical representation. A.N., A.I. and C.B. designed, performed and analyzed *in vitro* electrophysiological experiments. V.T.Q.L.-S. and I.J. performed immunohistochemical experiments. V.T.Q.L.-S. performed immunoblotting experiments. V.T.Q.L.-S., A.M., R.E. and F.M. acquired and analyzed behavioral data. F.M., D.I. and S.L.M. performed statistical analysis. All coauthors contributed to the revision of the manuscript.

1. Kwan, P., Schachter, S. & Brodie, M. Drug-resistant epilepsy. *N. Engl. J. Med.* **365**, 919–926 (2011).
2. Ben-Ari, Y. & Holmes, G.L. Effects of seizures on developmental processes in the immature brain. *Lancet* **5**, 1055–1063 (2006).
3. Turrigiano, G.G. & Nelson, S.B. Homeostatic plasticity in the developing nervous system. *Nat. Rev. Neurosci.* **5**, 97–107 (2004).
4. Lewis, D.A. & Levitt, P. Schizophrenia as a disorder of neurodevelopment. *Annu. Rev. Neurosci.* **25**, 409–432 (2002).
5. Allin, M. *et al.* Personality in young adults who are born preterm. *Pediatrics* **117**, 309–316 (2006).
6. Hensch, T.K. Critical period regulation. *Annu. Rev. Neurosci.* **27**, 549–579 (2004).
7. Katagiri, H., Fagiolini, M. & Hensch, T.K. Optimization of somatic inhibition at critical period onset in mouse visual cortex. *Neuron* **53**, 805–812 (2007).
8. Levelt, C.N. & Hübener, M. Critical-period plasticity in the visual cortex. *Annu. Rev. Neurosci.* **35**, 309–330 (2012).
9. Peters, H.C., Hu, H., Pongs, O., Storm, J.F. & Isbrandt, D. Conditional transgenic suppression of M channels in mouse brain reveals functions in neuronal excitability, resonance and behavior. *Nat. Neurosci.* **8**, 51–60 (2005).
10. Brown, D.A. & Passmore, G.M. Neural KCNQ (Kv7) channels. *Br. J. Pharmacol.* **156**, 1185–1195 (2009).
11. Wang, H.S. *et al.* KCNQ2 and KCNQ3 potassium channel subunits: molecular correlates of the M channel. *Science* **282**, 1890–1893 (1998).
12. Cooper, E.C., Harrington, E., Jan, Y.N. & Jan, L.Y. M channel KCNQ2 subunits are localized to key sites for control of neuronal network oscillations and synchronization in mouse brain. *J. Neurosci.* **21**, 9529–9540 (2001).
13. Devaux, J.J., Kleopa, K.A., Cooper, E.C. & Scherer, S.S. KCNQ2 is a nodal K+ channel. *J. Neurosci.* **24**, 1236–1244 (2004).
14. Biervert, C. *et al.* A potassium channel mutation in neonatal human epilepsy. *Science* **279**, 403–406 (1998).
15. Singh, N.A. *et al.* A novel potassium channel gene, *KCNQ2*, is mutated in an inherited epilepsy of newborns. *Nat. Genet.* **18**, 25–29 (1998).
16. Charlier, C. *et al.* A pore mutation in a novel KQT-like potassium channel gene in an idiopathic epilepsy family. *Nat. Genet.* **18**, 53–55 (1998).
17. Neubauer, B.A. *et al.* *KCNQ2* and *KCNQ3* mutations contribute to different idiopathic epilepsy syndromes. *Neurology* **71**, 177–183 (2008).
18. Weckhuysen, S. *et al.* KCNQ2 encephalopathy: emerging phenotype of a neonatal epileptic encephalopathy. *Ann. Neurol.* **71**, 15–25 (2012).
19. Orhan, G. *et al.* Dominant-negative effects of *KCNQ2* mutations are associated with epileptic encephalopathy. *Ann. Neurol.* **75**, 382–394 (2014).
20. Booth, D. & Evans, D.J. Anticonvulsants for neonates with seizures. *Cochrane Database Syst. Rev.* CD004218 (2004).
21. Evans, D.J., Levene, M.I. & Tsakmakis, M. Anticonvulsants for preventing mortality and morbidity in full term newborns with perinatal asphyxia. *Cochrane Database Syst. Rev.* CD001240 (2007).
22. Koyama, R. *et al.* GABAergic excitation after febrile seizures induces ectopic granule cells and adult epilepsy. *Nat. Med.* **18**, 1271–1278 (2012).
23. Dzhala, V.I. *et al.* NKCC1 transporter facilitates seizures in the developing brain. *Nat. Med.* **11**, 1205–1213 (2005).
24. Dzhala, V.I., Brumback, A.C. & Staley, K.J. Bumetanide enhances phenobarbital efficacy in a neonatal seizure model. *Ann. Neurol.* **63**, 222–235 (2008).
25. Wang, D.D. & Kriegstein, R. GABA regulates excitatory synapse formation in the neocortex via NMDA receptor activation. *J. Neurosci.* **28**, 5547–5558 (2008).
26. Kilb, W., Sinning, A. & Luhmann, H.J. Model-specific effects of bumetanide on epileptiform activity in the *in vitro*–intact hippocampus of the newborn mouse. *Neuropharmacology* **53**, 524–533 (2007).
27. Margineanu, D.G. & Klitgaard, H. Differential effects of cation-chloride cotransport-blocking diuretics in a rat hippocampal slice model of epilepsy. *Epilepsy Res.* **69**, 93–99 (2006).
28. Liu, Y., Shangguan, Y., Barks, J.D.E. & Silverstein, F.S. Bumetanide augments the neuroprotective efficacy of phenobarbital plus hypothermia in a neonatal hypoxia-ischemia model. *Pediatr. Res.* **71**, 559–565 (2012).
29. Kahle, K.T., Barnett, S.M., Sassower, K.C. & Staley, K.J. Decreased seizure activity in a human neonate treated with bumetanide, an inhibitor of the Na+-K+-2Cl− cotransporter NKCC1. *J. Child Neurol.* **24**, 572–576 (2009).
30. Pressler, R.M. *et al.* Bumetanide for the treatment of seizures in newborn babies with hypoxic ischaemic encephalopathy (NEMO): an open-label, dose-finding and feasibility phase 1/2 trial. *Lancet Neurol.* **14**, 469–477 (2015).
31. Khazipov, R. *et al.* Early motor activity drives spindle bursts in the developing somatosensory cortex. *Nature* **432**, 758–761 (2004).
32. Ben-Ari, Y. Developing networks play a similar melody. *Trends Neurosci.* **24**, 353–360 (2001).
33. Hanganu, I.L., Ben-Ari, Y. & Khazipov, R. Retinal waves trigger spindle bursts in the neonatal rat visual cortex. *J. Neurosci.* **26**, 6728–6736 (2006).
34. Weber, Y.G. *et al.* Immunohistochemical analysis of KCNQ2 potassium channels in adult and developing mouse brain. *Brain Res.* **1077**, 1–6 (2006).

35. Safiulina, V.F., Zacchi, P., Taglialatela, M., Yaari, Y. & Cherubini, E. Low expression of Kv7-M channels facilitates intrinsic and network bursting in the developing rat hippocampus. *J. Physiol. (Lond.)* **586**, 5437–5453 (2008).

36. Bullitt, E. Expression of c-fos–like protein as a marker for neuronal activity following noxious stimulation in the rat. *J. Comp. Neurol.* **296**, 517–530 (1990).

37. Streit, W.J. & Kreutzberg, G.W. Lectin binding by resting and reactive microglia. *J. Neurocytol.* **16**, 249–260 (1987).

38. Khalilov, I. *et al.* A novel *in vitro* preparation: the intact hippocampal formation. *Neuron* **19**, 743–749 (1997).

39. Ben-Ari, Y., Cherubini, E., Corradetti, R. & Gaiarsa, J.-L.L. Giant synaptic potentials in immature rat CA3 hippocampal neurons. *J. Physiol. (Lond.)* **416**, 303–325 (1989).

40. Leinekugel, X. *et al.* Correlated bursts of activity in the neonatal hippocampus *in vivo*. *Science* **296**, 2049–2052 (2002).

41. Seelke, A.M.H. & Blumberg, M.S. Developmental appearance and disappearance of cortical events and oscillations in infant rats. *Brain Res.* **1324**, 34–42 (2010).

42. Vanhatalo, S. & Kaila, K. Development of neonatal EEG activity: from phenomenology to physiology. *Semin. Fetal Neonatal Med.* **11**, 471–478 (2006).

43. Ben-Ari, Y. Excitatory actions of GABA during development: the nature of the nurture. *Nat. Rev. Neurosci.* **3**, 728–739 (2002).

44. Wang, D.D & Kriegstein, A.R. Blocking early GABA depolarization with bumetanide results in permanent alterations in cortical circuits and sensorimotor gating deficits. *Cereb. Cortex* **21**, 574–587 (2011).

45. Talos, D.M. *et al.* Antiepileptic effects of levetiracetam in a rodent neonatal seizure model. *Pediatr. Res.* **73**, 24–30 (2013).

46. Noebels, J.L. & Sidman, R.L. Inherited epilepsy: spike-wave and focal motor seizures in the mutant mouse tottering. *Science* **204**, 1334–1336 (1979).

47. Ryan, L.J. & Sharpless, S.K. Genetically determined spontaneous and brief spindle episodes in mice. *Exp. Neurol.* **66**, 493–508 (1979).

48. Vanhatalo, S., Hellström-Westas, L. & de Vries, L.S. Bumetanide for neonatal seizures: based on evidence or enthusiasm? *Epilepsia* **50**, 1292–1293 (2009).

49. Chabwine, J.N. & Vanden Eijnden, S. A claim for caution in the use of promising bumetanide to treat neonatal seizures. *J. Child Neurol.* **26**, 657–658 (2011).

50. Töpfer, M. *et al.* Consequences of inhibition of bumetanide metabolism in rodents on brain penetration and effects of bumetanide in chronic models of epilepsy. *Eur. J. Neurosci.* **39**, 673–687 (2014).

51. Löscher, W., Puskarjov, M. & Kaila, K. Cation-chloride cotransporters NKCC1 and KCC2 as potential targets for novel antiepileptic and antiepileptogenic treatments. *Neuropharmacology* **69**, 62–74 (2013).

52. Puskarjov, M., Kahle, K.T., Ruusuvuori, E. & Kaila, K. Pharmacotherapeutic targeting of cation-chloride cotransporters in neonatal seizures. *Epilepsia* **55**, 806–818 (2014).

53. Minlebaev, M., Ben-Ari, Y.Y. & Khazipov, R. Network mechanisms of spindle-burst oscillations in the neonatal rat barrel cortex *in vivo*. *J. Neurophysiol.* **97**, 692–700 (2007).

54. Rheims, S. *et al.* Layer-specific generation and propagation of seizures in slices of developing neocortex: role of excitatory GABAergic synapses. *J. Neurophysiol.* **100**, 620–628 (2008).

55. Tyzio, R. *et al.* Oxytocin-mediated GABA inhibition during delivery attenuates autism pathogenesis in rodent offspring. *Science* **343**, 675–679 (2014).

56. Deidda, G. *et al.* Reversing excitatory $GABA_AR$ signaling restores synaptic plasticity and memory in a mouse model of Down syndrome. *Nat. Med.* **21**, 318–326 (2015).

57. Dzhala, V.I., Saponjian, Y., De Konnick, Y. & Staley, K. Modulation of NKCC1 and KCC2 cotransporters for control of catastrophic drug-resistant seizures. (Program no. 521.05, 2014 Neuroscience Meeting Planner) (Society for Neuroscience, Washington, DC, 2014).

58. Huberfeld, G., Wittner, L. & Clemenceau, S. Perturbed chloride homeostasis and GABAergic signaling in human temporal lobe epilepsy. *J. Neurosci.* **27**, 9866–9873 (2007).

59. Miles, R., Blaesse, P., Huberfeld, G., Wittner, L. & Kaila, K. in *Jasper's Basic Mechanisms of the Epilepsies* 4th edn. (eds. Noebels, J.L., Avoli, M., Rogawski, M.A., Olsen, R.W. & Delgado-Escueta, A.V.) 1–13 (National Center for Biotechnology Information, Bethesda, MD, USA) (2012).

ONLINE METHODS

Animals and animal handling. Transgenic mice carrying *TRE-KCNQ2*[G279S] (C57BL/6J-Tg(*tetO-KCNQ2*[G279S])AIsb) were cross-bred with a line expressing the regulative tetracycline-responsive transcriptional activator (tTA) under the control of the prion protein promoter (FVB-Tg(*Prnp-tTA*)F959Sbp/J)[9,60]. Most experiments were performed with male (FVB × C57BL/6J)F1 littermates; for experiments in **Figures 2a–c, 4** and **6d,e** and **Supplementary Figures 6** and **8**, male (FVB × C57BL/6J × Crl:CD1)) F₁ littermates were also used. Double-transgenic (mutant) male mice and male littermates carrying only the *Prnp-tTA* transgene (controls) were housed together in standard mouse cages on wood bedding under conventional laboratory conditions (12-h dark and 12-h light cycle, constant temperature, constant humidity, and food (V1536, ssniff Spezialdiäten GmbH) and water *ad libitum*). All behavioral tests were performed during the dark cycle. Generation, care and use of the animals were in accordance with institutional guidelines. All experimental procedures were in accordance with the German Law for the Protection of Experimental Animals and the INSERM guidelines for experimental animal care and use, and they complied with the regulations of the US National Institutes of Health and the Society for Neuroscience (USA). All animal experiments were approved by the respective local authorities (Behörde für Soziales, Familie, Gesundheit und Verbraucherschutz der Freien und Hansestadt Hamburg (Germany), the Landesamt für Natur-, Umwelt- und Verbraucherschutz NRW, Recklinghausen (Germany), and the Ministère de l'Enseignement Supérieur et de le Recherche, Paris (France)).

***In situ* hybridization.** E17.5 embryo sections were hybridized with a human *KCNQ2*-specific 181-bp-long, [³²S]UTP-labeled probe corresponding to nucleotides 1374–1584 of the human *KCNQ2* open reading frame, according to standard techniques.

Pharmacological treatment. From P0–14, single- and double-transgenic mice were subcutaneously injected twice daily with 0.2 mg/kg bumetanide (Sigma) or with the solvent solution (vehicle) by an experimenter blinded to the genotype. Bumetanide or Burinex (LEO Pharma, France) was diluted in physiological saline just before injection. Alternative P0–P14 subcutaneous treatments included levetiracetam (Keppra; UCB Pharmaceuticals), titrated over the first 2 d up to 100 mg/kg (also injected twice a day), or picrotoxin (Sigma), which was administered once a day at 0.1 mg/kg.

Perfusion and slice preparation. Mice were deeply anesthetized and transcardially perfused first with phosphate-buffered saline and then with 4% paraformaldehyde. Brains were removed and post-fixed overnight at 4 °C. Serial coronal sections (50 μm thick) were prepared with a vibratome (Leica).

Nissl staining. Mounted and dried sections were stained with cresyl violet (Sigma) for Nissl substance.

Immunohistochemistry. To reduce free aldehydes, free-floating sections were incubated in 1% sodium borohydride. Endogenous peroxidases were quenched by incubation in 0.3% H_2O_2. Nonspecific interactions were blocked by using 10% horse serum, 0.2% BSA and 0.5% Triton X-100 in PBS. Antibodies were used at a dilution of 1:200 for anti-c-Fos (sc-52, Santa Cruz), 1:1,000 for anti-GFAP (clone GA5, Millipore) and at 20 μg/ml biotinylated *Griffonia simplifolia* lectin/isolectin B4 (B-1205, Vector Laboratories). Secondary biotinylated antibodies were diluted 1:1,000. Visualization of immunostainings was carried out using a streptavidin–horseradish peroxidase complex (Vector) combined with a diaminobenzidine substrate (DAB substrate, Sigma). Light microscopic analysis was performed using an Axioskop 2 (Zeiss) microscope with an AxioCam HRc camera. AxioVision (Zeiss) was used for image collection. Quantification of c-Fos⁺ neurons was performed using ImageJ[61].

Protein isolation and western blot analysis. Isolated hippocampi were homogenized in 300 mM sucrose, 20 mM MOPS and 1 mM EDTA, containing protease inhibitor mix (Sigma-Aldrich). Proteins were separated on NuPAGE 4–12% Bis-Tris gels (Invitrogen) in NuPAGE MOPS SDS running buffer (Invitrogen), electrophoretically transferred to PROTRAN nitrocellulose membranes (Whatman) and processed according to the antibody suppliers' recommendations (GFAP (clone GA5, Millipore; 1:1,000 dilution); synaptophysin (clone 7.2, Synaptic Systems; 1:1,000 dilution)).

Slice preparation and patch-clamp recordings. Neonatal P5–P8 mice were decapitated and the brains rapidly transferred to ice-cold sucrose solution (85 mM NaCl, 1.25 mM NaHPO₄, 2.5 mM KCl, 0.5 mM CaCl₂, 4 mM MgCl₂, 25 mM glucose, 75 mM sucrose, 25 mM NaHCO₃) oxygenated with carbogen (95% O₂ and 5% CO₂). Coronal sections (250 μm) were cut with a vibratome (Leica VT1200s), incubated for at least 30 min in 31–33 °C sucrose solution and then transferred to artificial cerebrospinal fluid (ACSF; 126 mM NaCl, 1.25 mM NaHPO₄, 2.5 mM KCl, 2 mM CaCl₂, 2 mM MgCl₂, 25 mM glucose, 25 mM NaHCO₃) at room temperature (20–22 °C). For electrophysiological recordings, slices were transferred to a chamber continuously perfused with ACSF at room temperature, except for GDPs, which were recorded at 31–33 °C. Intracellular solutions contained: 120 mM KMeSO₄, 20 mM KCl, 2 mM MgCl₂, 10 mM HEPES, 0.2 mM EGTA, 4 mM sodium-ATP, 0.3 mM Tris-GTP, 14 mM Tris-phosphocreatine, pH 7.3 with KOH, except for intracellular solutions for GDP recordings, which contained: 140 mM CsCl₂, 10 mM HEPES, 2 mM MgCl₂, 3 mM QX-bromide, pH 7.2 with cesium hydroxide. Whole-cell patch-clamp recordings were filtered at 4 kHz and digitized at 10 kHz using an EPC10 amplifier and PULSE software (HEKA).

CA1 pyramidal cells were voltage-clamped from a holding potential of −80 mV to test potentials of −70 to −20 mV in steps of 10 mV, and M currents were obtained by subtraction of current traces in the presence of 10 μM XE991 from current traces under control conditions. For current-clamp recordings, cells were held at −60 mV and depolarized by injections of 10–100 pA in steps of 10 pA. To determine spontaneous neonatal network activity, a modified ACSF containing 1 mM Mg²⁺ and 3.5 mM K⁺ was used. CA3 pyramidal neurons were voltage-clamped to −60 mV and recorded for up to 18 min. GDPs were defined as events with a minimum amplitude of 200 pA and a minimum length of 250 ms, and were binned in 3-min intervals. The baseline period was 6 min, and the pharmacological effect of XE991 was determined after bath application of more than 6 min.

***In toto* hippocampal recordings.** Experiments were performed on the intact hippocampi taken from mice at postnatal days 13–16. Animals were decapitated and brains were removed from the skull at 4 °C. The two hemispheres were separated and dissected to obtain intact hippocampi. Each hippocampus was placed in oxygenated (95% O₂ and 5% CO₂) ACSF with the following composition: 126 mM NaCl, 3.5 mM KCl, 2 mM CaCl₂, 1.3 mM MgCl₂, 25 mM NaHCO₃, 1.2 mM NaHPO₄, 10 mM glucose, pH 7.3. After a 3-h incubation at room temperature, hippocampi were transferred to the recording chamber, where they were fully submerged and superfused (perfusion rate of 10 ml/min) with warmed (33 °C) oxygenated ACSF. LFP recordings were made using extracellular glass electrodes that were filled with ACSF and placed in the temporal CA1 area. Field potentials were amplified with a DAM-80 AC amplifier (World Precision Instruments, FL, USA) and acquired using a Digidata 1200B card (Molecular Devices, CA, USA). Data were analyzed using ClampFit software (Molecular Devices, CA, USA).

***In vivo* depth recordings.** P5–P7 or P10–P11 neonatal mice were anesthetized with 1.5–2% isoflurane in 100% oxygen. A midline skin incision was made on the top of the skull. The periosteum was then denatured by a short treatment with 10% H₂O₂ and subsequently removed. The skull bone was rinsed with 0.9% NaCl solution and dried. Skin incisions were treated with a bupivacaine solution (Bucain-Actavis 0.25%). Local anesthesia around the surgical and fixation areas was used to minimize duress while avoiding the dampening effects of general anesthesia on neonatal brain activity[62]. For a common ground and reference electrode, a hole was drilled above the cerebellum. A silver wire was inserted and fixed with dental cement. For the cortical (V1) and hippocampal silicon probes, burr holes were placed at the following stereotaxic coordinates[63]: V1 2.42 mm posterior to bregma and 1.8 mm left to the midline; hippocampus 1.1 mm (P5–P7) or 1.6–1.9 mm (P10–P11) posterior to bregma and 1.5–1.6 mm left of the midline. Isoflurane anesthesia was discontinued after surgery. During recording, the mice were head-fixed and resting in the stereotaxic instrument. Body temperature was maintained at the ambient nest temperature of about 34 °C

using a homeothermic heating pad (Stoelting). At P5–P7, linear 16-site silicon probes with a distance of 50 or 100 μm between recording sites (A1×16-50/100-5mm-703-A16, NeuroNexus Technologies) were inserted into the V1 cortex with a lateral tilt of 10° and vertically into the dorsal hippocampus along the CA1 to CA3 or DG axis. Sparse unit firing and the geometry and impedance of the silicon probes, which were optimized to record LFP depth profiles, precluded the quantification of unit activity in the data set from P5–P7 neonates. Therefore, we recorded extracellular unit firing from slightly older, P10–P11, animals with electrodes optimized to isolate single units (four-shank silicon probes with eight electrode sites per shank (Buzsaki-32L), or linear 32-site electrodes with a distance of 25 μm between recording sites (A1x32-6mm-25-177-A32), both from NeuroNexus Technologies, USA). The silicon probes were connected to a unity gain buffer amplifier (HS-18 or HS-36 headstage, Neuralynx, Inc., USA) mounted to the stereotaxic instrument (Stoelting). Data were digitally filtered (0.5- to 9,000-Hz bandpass) and digitized as 16-bit integers with a sampling rate of 32 kHz using a Digital Lynx data acquisition system (Neuralynx, Inc., USA). Animal movements were detected by a piezoelectric sensor placed under the animal's thorax and recorded in parallel with the same sampling rate. Data acquisition was started about 15–30 min after probe insertion when recording conditions were stable. Probe positions were marked by silicon probes covered by the fluorescence dye DiI and verified in NeuroTrace fluorescent Nissl-stained (Invitrogen) coronal slices (**Supplementary Fig. 4**).

***In vivo* data analysis.** All *in vivo* data were analyzed and visualized in Matlab (Mathworks) or Neuroscope (http://neuroscope.sourceforge.net/)[64]. LFPs were low-pass–filtered and downsampled to 1.25 kHz from raw traces; CSDs were built from the second spatial derivative of 1- to 200-Hz–filtered LFPs. Sharp waves (SPWs) were considered the point of maximum negativity in deep hippocampus after automatically detecting high variance across CSD traces; SPW amplitudes were quantified by max. peak to min. trough in the LFP. Hippocampal beta oscillations (HBOs), cortical spindle bursts and slow activity transients were marked by hand and verified by independent observers. Multitaper spectrograms of original and whitened signals were computed using Chronux (http://www.chronux.org) for scoring and HBO peak estimation; for visualization, wavelets (Gabor family) were also used. HBO peaks were defined as the max of the average whitened event spectra detected between 4 and 40 Hz, after normalizing by the whitened spectra of the overall recording (limited to the first 60 min per animal and excluding twitch movement periods.) Blue to red edges of the jet color map correspond to 10 and 40 dB (multitaper estimate of) power of the mV/mm² CSD trace in **Figure 2d**; the color map edges span the upper 99.9% of the range of wavelet coefficients of the mV LFP in **Figure 2e** (left). In **Figure 6d** the jet color map spanned 28 or 38 dB power for the upper (multitaper) visualizations, or the lower 99.5% of wavelet coefficients for the zoom-ins below. Traces were plotted, unfiltered, for **Figure 2a**, and after low-pass filtering for display purposes in **Figures 2e** (right) and **6d**.

Unit analysis. Spike extraction was performed on thresholded high-passed (800 Hz) or median-filtered (23-sample window) 32-kHz raw signal, using either spikeDetekt[65] or ND Manager plug-ins[64]. Spikes were clustered into putative units with KlustaKwik[66] and manually corrected off-line using Klusters[64]. Of 930 isolated units, 599 were deemed suitable for analysis on the basis of a combination of rate, clean waveforms and refractory period ($n = 151$ from eight vehicle-treated controls; $n = 186$ from seven bumetanide-treated controls; $n = 117$ from five vehicle-treated mutants; $n = 145$ from eight bumetanide-treated mutants). Of these cells, 337 were found to have an ACG peak below 25 ms, defined as a maxima more than three times the ACG asymptote expected from a Poisson process of the given rate (in practice, 98% of ACG peaks were ten or more times larger, and all appeared within the first 3–12 ms). For visualization, ACGs were scaled along the *y* axis to their respective maximums and plotted on a log-scale *x* axis (bin size was 1 ms.) Triplets and quadruplets were detected as sequences of spikes with each interspike interval between 2 and 15 ms, and values were reported as the percentage of a unit's spikes participating in one or more such sequences. In the data in the supplementary information (**Supplementary Fig. 8**), bursting results were confirmed with an alternative definition that counted percentage of *n* (4 or 5) spikes occurring within windows of a given size (60 or 75 ms).

Telemetric recordings. Telemetric ECoG analyses were performed using implantable radio transmitters (models TA11EA-F20 or TA11ETA-F20, DataSciences International). Adult (at least 3 months old) male mice received 0.05 mg/kg buprenorphine (subcutaneously) for analgesia and were anesthetized with 1.5–2% isoflurane in 100% oxygen. Midline skin incisions were made on the top of the skull and in the neck. The transmitter body was implanted subcutaneously. The tips of the EEG leads were placed 2 mm posterior to lambda and 1.8 mm right to the midline for the recording electrode, and 1 mm posterior to lambda and 1–2 mm left to the midline for the reference electrode. The electrodes were fixed with dental cement. Radio transmitters allowed simultaneous monitoring of ECoG and motor activity in undisturbed, freely moving mice that were housed in their home cages. Telemetry data and corresponding video data were recorded 1 week after surgery at the earliest and were stored digitally using Ponemah software (version 5.1, Data Sciences International, USA). The control group consisted of naive mice ($n = 4$) and mice that had received neonatal bumetanide treatment ($n = 3$). The mutants had received either vehicle or bumetanide treatment as neonates. Hypersynchronous events in the 5- to 10-Hz theta frequency band were autodetected by a sliding window threshold of more than 1.5 times the power detected in the theta band during a rapid-eye-movement (REM) sleep episode of the same mouse and was manually inspected (Neuroscore 3, DataSciences International).

Behavior. Neonatal reflex tests were used to assess early sensorimotor development[67]. Mice were tested once daily from postnatal days 1 to 8, and scored twice with maximum trial duration and inter-trial intervals of 30 s. The righting reflex (surface righting) was tested with respect to a successful turn from the back to all four paws. For cliff avoidance behavior, mice were placed with the nose above the edge of an elevated plate and tested for an avoidance reaction by turning the body 90° away from the edge. For the geotactic reflex, mice were placed on an inclined Plexiglas plate with the nose pointing down and tested for the ability to turn 180°.

Open-field activity was analyzed during the dark cycle using a protocol consisting of a 5-min adaptation period and one 15-min trial in light beam boxes (50 × 50 × 40 cm, TSE Systems). Circadian activity was monitored using an infrared motion detector system (Infra-e-motion)[9]. Motor function was assessed using the rotarod and pole tests[68]. Strength of the forelimbs was measured using the Grip Strength Meter system (TSE Systems)[69]. Cognitive abilities were tested in the Y maze spontaneous alternation, contextual fear conditioning and water maze tests. In the Y maze spontaneous alternation test, mice were placed into the center of a Plexiglas Y maze with three 40-cm-long equiangular arms. Entries into the arms were counted when the hind limbs reached a mark delineated 5 cm on the inside of the arm. Novel arm choices were recorded. After 25 novel choices the animal was placed back into the home cage. Contextual fear conditioning[70] was performed as follows: the conditioned response was analyzed by quantifying the percentage of time spent freezing (defined as the absence of body movements for at least 1 s). Freezing behavior was automatically analyzed using a modified version of the Mouse-E-Motion system (Infra-e-motion). The water maze consisted of a circular tank (145 cm in diameter). Three days before the start of the experiment, mice were familiarized with swimming and climbing onto a platform (diameter of 10 cm) that was placed in a small rectangular maze (42.5 cm × 26.5 cm, and 15.5 cm high)[71]. On experimental days 1 and 2, mice were trained in the water maze (four trials per day, inter-trial interval of 20 min). Four starting positions were pseudo-randomized. Animals were released into the water facing the wall and were allowed to find the platform within 90 s and to climb onto it. After staying on the platform for 10 s, the mice were returned to their home cage and warmed under an infrared heat lamp. Twenty-four hours after the last trial, mice underwent a 60-s transfer trial during which the platform was removed. The time spent in the four quadrants was analyzed with the software EthoVision (Noldus)[72].

Statistics. Unless specified otherwise, group measures are given as mean ± s.e.m.; error bars also indicate s.e.m. The difference between genotypes or between control and test conditions was assessed using Student's *t*-test or Mann-Whitney *U* test. Unless stated otherwise, differences between more than two groups or multifactorial designs were tested with one-, two- or three-way analysis of variance (ANOVA), respectively, followed by the Newman-Keuls post hoc test

or the Kruskal-Wallis multiple comparisons test as appropriate (Statistica 7, Statsoft). ANOVA F ratio degrees of freedom are listed as $F_{x,y}$ in the text and legends for the nominator (x) and denominator (y). The Wilcoxon signed-rank test (GraphPad Prism 5) was used to assess the alternation ratio in the Y maze test and entries into the target in the rectangular water maze test, with chance level at 50%. The significance level was set at $P < 0.05$. No randomization method was used, and no animal was excluded from analysis. For electrophysiological and behavioral experiments, investigators were blinded to the animals' genotypes, but not for allocation during histological and immunoblot experiments or outcome analysis. The sample size was chosen on the basis of our previous experience and the principles of the '3 Rs' (reduction, refinement and replacement); all n values are indicated in figure legends.

60. Tremblay, P., Meiner, Z., Galou, M. & Heinrich, C. Doxycycline control of prion protein transgene expression modulates prion disease in mice. *Proc. Natl. Acad. Sci. USA* **95**, 12580–12585 (1998).
61. Abràmoff, M.D., Magelhães, P.J. & Ram, S.J. Image processing with ImageJ. *Biophotonics Int.* **11**, 36–42 (2004).
62. Adelsberger, H., Garaschuk, O. & Konnerth, A. Cortical calcium waves in resting newborn mice. *Nat. Neurosci.* **8**, 988–990 (2005).
63. Paxinos, G., Hallyday, G., Watson, C., Koutcherov, Y. & Wang, H. *Atlas of the Developing Mouse Brain at E17.5, P0 and P6.* (Academic Press, 2007).
64. Hazan, L., Zugaro, M. & Buzsáki, G. Klusters, NeuroScope, NDManager: a free software suite for neurophysiological data processing and visualization. *J. Neurosci. Methods* **155**, 207–216 (2006).
65. Rossant, C. *et al.* Spike sorting for large, dense electrode arrays. *bioRxiv* http://biorxiv.org/content/biorxiv/early/2015/02/16/015198.full.pdf (2015).
66. Kadir, S.N., Goodman, D.F.M. & Harris, K.D. High-dimensional cluster analysis with the masked EM algorithm. *Neural Comput.* **26**, 2379–2394 (2014).
67. Heyser, C.J. Assessment of developmental milestones in rodents. *Curr. Protoc. Neurosci.* **25**, 8.18 (2003).
68. Freitag, S., Schachner, M. & Morellini, F. Behavioral alterations in mice deficient for the extracellular matrix glycoprotein tenascin-R. *Behav. Brain Res.* **145**, 189–207 (2003).
69. Morellini, F. & Schachner, M. Enhanced novelty-induced activity, reduced anxiety, delayed resynchronization to daylight reversal and weaker muscle strength in tenascin-C–deficient mice. *Eur. J. Neurosci.* **23**, 1255–1268 (2006).
70. Sawallisch, C. *et al.* The insulin receptor substrate of 53 kDa (IRSp53) limits hippocampal synaptic plasticity. *J. Biol. Chem.* **284**, 9225–9236 (2009).
71. Fellini, L., Schachner, M. & Morellini, F. Adult but not aged C57BL/6 male mice are capable of using geometry for orientation. *Learn. Mem.* **13**, 473–481 (2006).
72. Fellini, L. & Morellini, F. Geometric information is required for allothetic navigation in mice. *Behav. Brain Res.* **222**, 380–384 (2011).